International Journal of Engineering Science 122 (2018) 14–29

Contents lists available at ScienceDirect

International Journal of Engineering Science

journal homepage: www.elsevier.com/locate/ijengsci

Evaluation of the probability density of inhomogeneous fiber orientations by computed tomography and its application to the calculation of the effective properties of a fiber-reinforced composite

Tatiana Mishurova[a], Natalia Rachmatulin[a], Patrick Fontana[a], Tyler Oesch[a], Giovanni Bruno[a], Enrico Radi[b], Igor Sevostianov[c,d,*]

[a] BAM, Bundesanstalt für Materialforschung und –Prüfung, Unter den Eichen 87, Berlin 12205, Germany
[b] Dipartimento di Scienze e Metodi dell'Ingegneria, Università di Modena e Reggio Emilia, Via Amendola, 2 Reggio Emilia 42122, Italy
[c] Department of Mechanical and Aerospace Engineering, New Mexico State University, Las Cruces, NM 88001, USA
[d] Center for Design, Manufacturing, and Materials, Skolkovo Institute of Science and Technology, Skolkovo, Russia

ARTICLE INFO

Article history:
Received 5 October 2017
Revised 18 October 2017
Accepted 22 October 2017

Keywords:
Computed tomography
Orientation distribution
Effective properties
Fiber-reinforced composite

ABSTRACT

This paper focuses on the experimental evaluation of one of the key microstructural parameters of a short-fiber reinforced composite – the orientation distribution of fibers. It is shown that computed tomography (CT) produces results suitable for reconstruction of the orientation distribution function. This function is used for calculation of the effective elastic properties of polymer-fiber reinforced concrete. Explicit formulas are derived for overall elastic moduli accounting for orientation distribution in the frameworks of the non-interaction approximation, the Mori–Tanaka–Benveniste scheme, and the Maxwell scheme. The approach illustrated can be applied to any kind of composite material.

1. Introduction

1.1. Contribution of fiber distribution and orientation characteristics to composite performance

Although the performance of components made from composite materials, and in particular from concrete, is still commonly simulated using macroscale models that treat these materials as homogeneous media, recent research has made it clear that in order to accurately simulate the response of concrete, models which adequately account for concrete heterogeneity will be required (Cusatis, Pelessone, & Mencarelli, 2011). This is because even at service loads, concrete cracking patterns are highly dependent on material heterogeneity (Cusatis & Nakamura, 2011). Previous research has demonstrated that both spatial arrangement and fiber orientations have a great impact on the strength of fiber-reinforced concrete members (Barnett et al., 2010; Ferrara & Meda, 2006; Pujadas, Blanco, Cavalaro, de la Fuente, and Aguado, 2014a; Oesch, 2015). These fiber orientations are often highly anisotropic in nature and are the result of material flow patterns during the casting process (di Prisco, Ferrara, & Lamperti, 2013; Pujadas et al., 2014a; Oesch, 2015).

* Corresponding author.
E-mail address: igor@nmsu.edu (I. Sevostianov).

https://doi.org/10.1016/j.ijengsci.2017.10.002
0020-7225/

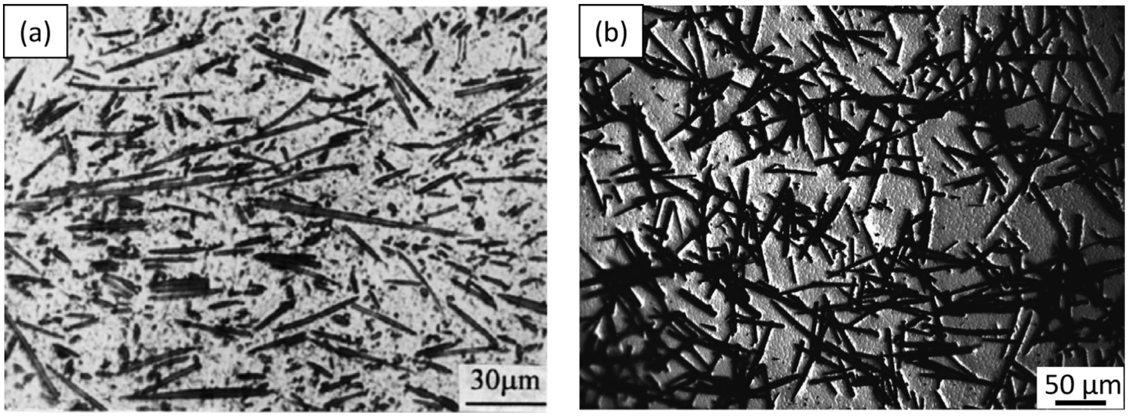

Fig. 1. Optical micrographs showing the orientation distribution of fibers in: (a) and Al2O3 fiber-reinforced aluminum alloy (from Kang, Yang, & Zhang, 2002); (b) polypyrrole-coated amorphous silica short fiber reinforced polyvinylidene fluoride matrix (from Arenhart, Barra, & Fernandes, 2015).

These anisotropic characteristics of fiber-reinforced concrete have major safety implications for its widespread use. Material anisotropy can lead to planes of weakness within structural members. When not properly controlled, these weak planes can become aligned with the primary plane of stress and cause premature failure. The analysis of these fiber orientation characteristics and their implementation into finite element analysis models will serve as an important first step towards obtaining a better understanding of how the characteristics of concrete component materials and casting methods affect material structure and performance.

1.2. Analytical methodologies proposed to account for anisotropic fiber orientation distribution

The present paper focuses on the integration of CT data into micromechanical homogenization techniques to account for orientation distribution of non-spherical inhomogeneities in heterogeneous materials. In short-fiber reinforced composites, the fibers are usually neither perfectly parallel, nor perfectly randomly oriented, but have a certain orientation distribution (Fig. 1), which is one of the primary factors affecting the overall mechanical properties (Kachanov & Sevostianov, 2005). However, non-spherical inhomogeneities in composites had typically been considered as perfectly aligned until the beginning of 1980s. The authors are not aware of analyses accounting for the random orientation of fibers prior to Chou and Nomura (1980–1981) and Takao, Chou, and Taya (1982), who applied an average induced strain approach to composites with 3D randomly oriented short fibers. The averaging procedure was later used by Benveniste (1987) and Chen, Dvorak, and Benveniste (1992) in the Mori–Tanaka scheme. Tandon and Weng (1986) considered two cases of random distribution of fibers: in-space (overall isotropy) and in-plane (overall transverse isotropy). The general case of the orientation distribution of short fibers was first discussed by Ferrari and Johnson (1989), who presented a theoretical scheme in which the fiber orientation distribution was allowed to be arbitrarily specified. These authors first introduced an orientation distribution function (ODF) defined over the full Euler space. This approach was implemented into the Mori–Tanaka scheme by Ferrari (1991) and Marzari and Ferrari (1992).

In the successive years many specific ODFs have been discussed in literature. During the analysis of a fiber-reinforced composite by Lu and Liaw (1995), independence of the orientation distribution of fibers was assumed with respect to different Euler angles $\phi, \theta, and\, \varphi$, so that:

$$P(\phi,\ \theta,\ \varphi) = P(\phi)P(\theta)P(\varphi) \quad (0 \le \phi,\ \theta,\ \varphi \le \pi) \tag{1.1}$$

They used a combination of Gaussian and trigonometric distributions which fit the distribution obtained by quantitative image analysis of SEM pictures:

$$P(\phi) = \frac{2 + \cos(2\phi)}{2\pi};$$
$$P(\theta) = \sqrt{\frac{2}{\pi}} \exp\left(\frac{-(\theta - \pi/2)^2}{2}\right);$$
$$P(\varphi) = \sqrt{\frac{2}{\pi}} \exp\left(\frac{-(\varphi - \pi/2)^2}{2}\right) \tag{1.2}$$

Applicability of this function to non-random orientation distribution is, however, unclear.

Chen and Wang (1996) calculated the effective thermal conductivity of a transversely isotropic composite containing misoriented inhomogeneities. The orientation distribution was described by:

$$P(\theta) = 1 - \exp(\lambda\theta) \tag{1.3}$$

where the zero value of the scatter parameter λ corresponds to random distribution of the inhomogeneities and high values indicate a highly oriented material.

A detailed analysis of the effect of the inclusion of orientation distribution on the effective thermomechanical properties of fiber-reinforced composites has been done by Pettermann, Bohm, and Rammerstorfer (1997), who used the Mori–Tanaka scheme and assumed the exponential ODF:

$$P(\theta) = \exp\left(-\theta^2/2\lambda^2\right) \tag{1.4}$$

This can be regarded as a truncated axisymmetric Gaussian distribution. These authors calculated the overall Young's moduli, the shear moduli and the coefficients of thermal expansion, as well as the onset of yielding of the matrix phase under thermal and mechanical loading conditions. Duschlbauer, Bohm, and Pettermann (2003) used this approach for calculation of the effective thermal properties of composites.

Fu and Lauke (1998) used a two-parameter ODF:

$$P(\theta) = \frac{(\sin\theta)^{2p-1}(\cos\theta)^{2q-1}}{\int_{\theta_{\min}}^{\theta_{\max}} (\sin\theta)^{2p-1}(\cos\theta)^{2q-1} d\theta};\ 0 \le \theta_{\min} \le \theta \le \theta_{\max} \le \pi/2 \tag{1.5}$$

where p and q are shape parameters which can be used to determine the shape of the distribution curves. A similar model (with only one parameter) was used by Zhupanska (2013) to calculate mechanical properties of buckypaper nanocomposite. Turner, Signorelli, Bertinetti, and Bolmaro (1999) used a Gaussian distribution for each Euler angle, assuming those distributions were statistically independent, and calculated effective mechanical properties and phase average stresses in SiC/Al composites. Similar approaches have been adopted by Fernandez et al. (2004) and Bruno and Fernandez (2007). Sevostianov and Kachanov (2000) considered the transversely isotropic orientation distribution of cracks and suggested the use of an ODF in the form:

$$P_\lambda(\varphi) = \frac{1}{2\pi}\left[\left(\lambda^2+1\right)e^{-\lambda\varphi} + \lambda e^{-\lambda\pi/2}\right] \tag{1.6}$$

This function was used later by Sevostianov, Levin, and Radi (2016) to calculate viscoelastic properties of short-fiber reinforced composites.

Kachanov, Tsukrov, and Shafiro (1994) showed that the form of the ODF does not noticeably affect the overall elastic and conductive properties of a composite. Thus the specific choice is mostly dictated by computational convenience. A more important issue is related to the experimental evaluation of the ODF and the incorporation of experimental data into analytical formulas. Certain progress in this direction has been obtained during the last decade.

1.3. Experimental techniques for determining the fiber orientation characteristics of materials

Dunn, Ledbetter, Heyliger, and Choi (1996) considered SiC/Al short-fiber reinforced composites and evaluated the ODF using neutron-diffraction techniques (suitable for monocrystalline fibers). They expanded the orientation-distribution function in a series of generalized spherical harmonics and suggested the use of the eighth-order transformation tensor relating a fourth-order tensor in the local and global coordinate systems. This approach was later used by Dunn and Ledbetter (1997, 2000) for the calculation of elastic-plastic and thermo-elastic properties of short-fiber reinforced composites and by Li (2000) for the calculation of piezoelectric properties. Pérez, Banda, and Ounaies (2008) determined the ODF in aligned single wall nanotube polymer nanocomposites using polarized Raman spectroscopy. Blanco (2013) analyzed various destructive and non-destructive methods for fiber orientation determination. Most of them are based on electrical resistivity and inductivity of fibers (see, for example, Lataste, Behloul, & Breysse, 2008), which are applicable for metallic fibers only.

Another possibility to evaluate fiber orientation distribution is analysis of 2D images obtained by different methods. The extraction of fiber orientation information from radiographs using the Fourier image transform was proposed in Redon, Chermant, Chermant, and Coster (1998,1999). Lee, Kim, Kim, and Kim (2009) suggested the use of digital image analysis. This technique was practically implemented by Kang, Lee, Kimc, and Kim (2011) and Kang and Kim (2012). One of the most widely used 2D methods for evaluation of fiber orientation is microscopy, which is used to evaluate the ODF based on analysis of cross sections (Tsuda et al., 2014). Clarke and Eberhardt (1999, 2001) and Zhu, Blumenthal, and Lowe (1997) showed that fiber orientation analysis can be performed by using confocal microscopy. However, microscopy methods are very time-consuming (Bay et al. 1992), and the precise relationship between 3D microstructure and 2D images is still unknown. Bernasconi, Cosmi, and Hine (2012) and Liu, Li, Liu, Cui, and Yang (2013), performed comparisons between 2D optical methods and CT. Their results show that CT measurements have higher accuracy in the evaluation of fiber orientation as compared to 2D image analysis. Suuronen, Kallonen, Eik, Puttonen, Serimaa, and Herrmann (2013) used CT measurements to study orientation distribution probability density in steel-fiber reinforced concrete. Pujadas et al. (2014a,b) discussed the link between the mechanical properties of fiber-reinforced concrete and the fiber orientation. In particularly, they demonstrated the efficiency of the CT technique for evaluating fiber orientation, but they did not perform orientation distribution probability density analysis, and consequently did not insert an ODF into their model.

In the present paper, CT reconstructions of a polymer-fiber reinforced concrete are used to evaluate the ODF (in the form given by Eq. (1.6)) and integrate the result into explicit expressions for effective elastic moduli of the material. This approach is based on the concept of property contribution tensors and is illustrated by using different homogenization schemes.

2. Calculation of the effective elastic properties of a composite with non-randomly oriented inhomogeneities

2.1. Background results – property contribution tensors

Property contribution tensors are used in the context of homogenization problems to describe the contribution of a single inhomogeneity to the property of interest – elasticity, thermal or electrical conductivity, diffusion coefficient, etc. In the context of the effective elastic properties, one can use the compliance contribution tensor of an inhomogeneity $\boldsymbol{H}$, which gives the extra strain produced by the introduction of the inhomogeneity in the otherwise uniform stress field, or the stiffness contribution tensor $\boldsymbol{N}$, which gives the extra stress due to the inhomogeneity when it is placed into the otherwise uniform strain field.

Compliance contribution tensors were first introduced in the context of pores and cracks by Horii and Nemat-Nasser (1983) (see also detailed discussion in the book of Nemat-Nasser & Hori, 1993). For the general case of elastic inhomogeneities, these tensors were given for ellipsoidal shapes by Sevostianov and Kachanov (1999, 2002). For the reader's convenience, a brief description of the property contribution tensors is provided below.

First a homogeneous *elastic* material (matrix) is considered, with compliance and stiffness tensors $\boldsymbol{S}^0$ and $\boldsymbol{C}^0$, assumed to be isotropic. The matrix contains an inhomogeneity, of volume $V^{(1)}$, of a different elastic material with compliance and stiffness tensors $\boldsymbol{S}^1$ and $\boldsymbol{C}^1$. The contribution of the inhomogeneity to the overall strain per representative volume V (the extra strain, as compared to the homogeneous matrix) is given by:

$$\Delta\,\boldsymbol{\varepsilon} = \frac{V^{(1)}}{V}\boldsymbol{H}{:}\boldsymbol{\sigma}^{\infty} \tag{2.1}$$

where $\boldsymbol{\sigma}^{\infty}$ is the "remotely applied" stress field that, in absence of the inhomogeneity, would have been uniform within its site (i.e., "homogeneous boundary conditions" as described by Hashin (1983)). The colon in Eq. (2.1) denotes contraction over two indices. Eq. (2.1) can also be inverted to provide the definition of the fourth-rank tensor $\boldsymbol{H}$ – the compliance contribution tensor of the inhomogeneity. In the case of multiple inhomogeneities, the extra compliance due to their presence is given by:

$$\Delta\,\boldsymbol{S} = \frac{1}{V}\sum V^{(k)*}\boldsymbol{H}^{(k)} \tag{2.2}$$

Alternatively, one can consider the extra average stress $\Delta\,\boldsymbol{\sigma}$ (over V) due to an inhomogeneity under uniform displacement boundary conditions (displacements on ∂V have the form $\boldsymbol{u}|_{\partial V} = \boldsymbol{\varepsilon}^0 \cdot \boldsymbol{n}$ where ε^0 is a constant tensor). This defines the stiffness contribution tensor $\boldsymbol{N}$ of an inhomogeneity:

$$\Delta\,\boldsymbol{\sigma} = \frac{V^{(1)}}{V}\boldsymbol{N}{:}\boldsymbol{\varepsilon}^0, \tag{2.3}$$

In the case of multiple inhomogeneities, the extra stiffness due to the inhomogeneities is given by:

$$\Delta\,\boldsymbol{C} = \frac{1}{V}\sum V^{(k)*}\boldsymbol{N}^{(k)} \tag{2.4}$$

The $\boldsymbol{H}$ and $\boldsymbol{N}$ tensors are determined by the shape of the inhomogeneity and are independent of its size. They also depend on the elastic constants of the matrix and of the inhomogeneity.

For an ellipsoidal inhomogeneity, the fourth-order tensors $\boldsymbol{H}$ and $\boldsymbol{N}$ can be expressed in terms of elastic contrast (i.e., the difference in stiffness $\boldsymbol{C}$ or compliance $\boldsymbol{S}$ of the matrix caused by inhomogeneity). The fourth-order Hill's tensors $\boldsymbol{P}$ and $\boldsymbol{Q}$, which describe the effects of the shape of the inhomogeneity are defined by the equations:

$$\boldsymbol{H} = \left[\left(\boldsymbol{S}^1 - \boldsymbol{S}^0\right)^{-1} + \boldsymbol{Q}\right]^{-1}; \quad \boldsymbol{N} = \left[\left(\boldsymbol{C}^1 - \boldsymbol{C}^0\right)^{-1} + \boldsymbol{P}\right]^{-1} \tag{2.5}$$

Note that the effects of the elastic contrast and shape of the inhomogeneity can be separated for ellipsoidal shapes. The fourth-order Hill's tensor $\boldsymbol{P}$ (Hill, 1965) is the integral over the volume of the inhomogeneity from the second gradient of Green's tensor. Tensor $\boldsymbol{Q}$ is related to $\boldsymbol{P}$ as follows (Walpole, 1966):

$$Q_{ijkl} = C^0_{ijmn}\left(J_{mnkl} - P_{mnrs}C^0_{rskl}\right) \tag{2.6}$$

Here, $J_{ijkl} = (\delta_{ik}\delta_{lj} + \delta_{il}\delta_{kj})/2$ and the inverse of symmetric (with respect to $i{\leftrightarrow}j$ and $k{\leftrightarrow}l$) fourth-order tensor X^{-1}_{ijkl} is defined by $X^{-1}_{ijmn}X_{mnkl} = X_{ijmn}X^{-1}_{mnkl} = J_{ijkl}$.

For a spheroidal inhomogeneity (with semi-axes $a_3;\ a_1 = a_2$) embedded in an isotropic matrix, it is convenient to use a representation of these tensors in terms of standard tensor bases $\boldsymbol{T}^{(1)}, \ldots, \boldsymbol{T}^{(6)}$ (see the Appendix for further details):

$$\boldsymbol{P} = \sum_{k=1}^{6} p_k\boldsymbol{T}^{(k)};\ \boldsymbol{Q} = \sum_{k=1}^{6} q_k\boldsymbol{T}^{(k)};\ \boldsymbol{H} = \sum_{k=1}^{6} h_k\boldsymbol{T}^{(k)};\ \boldsymbol{N} = \sum_{k=1}^{6} n_k\boldsymbol{T}^{(k)} \tag{2.7}$$

Thus, the determination of these tensors reduces to the calculation of factors p_k, q_k, h_k and n_k. The relations for these coefficients are given in the Appendix.

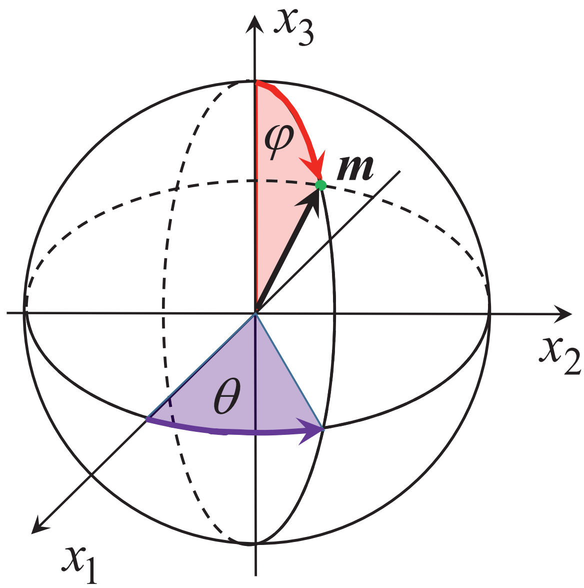

Fig. 2. Spherical coordinate system used in Eq. (2.9).

Remark. Generally, the $\boldsymbol{H}$ and $\boldsymbol{N}$ tensors in Eqs. (2.2) and (2.4) have to reflect the interactions between the inhomogeneities. However, incorporating interactions into the micromechanical parameter amounts to solving the interaction problem, and hence it is not practical. Contributions of individual inhomogeneities are taken into account by treating them as *non-interacting* (in particular, mutual positions of inhomogeneities are not reflected) and then using them in various approximate schemes that aim at accounting for interactions (such as effective media and effective field approaches).

2.2. Effective elastic stiffnesses

If the interaction between inhomogeneities is neglected, the change in the elastic compliances (or stiffnesses) due to the inhomogeneities is calculated using Eq. (2.2) (or Eq. (2.4)). If the inhomogeneities in a composite have the same shape, size, and properties and their orientation is described by a known ODF, it is convenient to replace the summation in $\Sigma V^{(k)*}\boldsymbol{H}^{(k)}$ and $\Sigma V^{(k)*}\boldsymbol{N}^{(k)}$ by averaging over the orientations, so that:

$$\boldsymbol{S} = \boldsymbol{S}_0 + c\langle \boldsymbol{H}\rangle ; \boldsymbol{C} = \boldsymbol{C}_0 + c\langle \boldsymbol{N}\rangle \tag{2.8}$$

where c is the volume fraction of the inhomogeneities.

Following Sevostianov and Kachanov (2000), the unit vector $\boldsymbol{m}$ is expressed along the ith spheroid's symmetry axis in terms of two angles $0 \le \phi \le \pi/2$ and $0 \le \theta \le 2\pi$ (Fig. 2):

$$\boldsymbol{m}(\varphi,\theta) = \cos\theta \sin\varphi\, \boldsymbol{e_1} + \sin\theta \sin\varphi\, \boldsymbol{e}_2 + \cos\varphi\, \boldsymbol{e}_3 \tag{2.9}$$

Eq. (2.9) contains terms related to the statistics of fiber orientation, in particular the probability density function $P(\varphi,\theta)$ defined on the upper semi-sphere of unit radius and subject to the normalization condition:

$$\int_0^{2\pi}\int_0^{\pi/2} P(\varphi,\theta)\sin\varphi d\varphi d\theta = 1 \tag{2.10}$$

The orientation distributions of fibers are assumed to be independent with respect to angles θ and φ so that $P(\varphi,\ \theta) = P(\varphi)P(\theta)$. These distributions also account for orientation characteristics that are distinguished by intermediate properties between the ideal random and the parallel cases. This is accomplished by specifying the following probability density function containing the scatter parameter ζ:

$$P_{\zeta_\varphi}(\varphi) = \left(\zeta_\varphi^2 + 1\right) e^{-\zeta_\varphi \varphi} + \zeta_\varphi e^{-\zeta_\varphi \pi/2}; P_{\zeta_\theta}(\theta) = \frac{\zeta_\theta}{2}\, e^{-\zeta_\theta ||\theta-\pi|-\pi|} + \frac{1}{2\pi} e^{-\zeta_\theta \pi} \tag{2.11}$$

The parameter ζ characterizes the sharpness of the peak and the extent of the scatter. The extreme cases of fully random and perfectly parallel fibers correspond to $\zeta = 0$ and $\zeta \to \infty$, respectively. Note that the effective elastic moduli are relatively insensitive to the exact form of a function that has the above-mentioned features (Kachanov et al., 1994). Fig. 3 shows the dependencies of $P_\zeta(\varphi)$ on φ and $P_\zeta(\theta)$ on θ for several values of ζ and the behavior of $P_\zeta(\varphi)\sin\varphi$. If parameter ζ is known, then the following two average orientation tensors can be evaluated:

$$A_{ij} = \langle m_i m_j\rangle ; \quad B_{ijkl} = \langle m_i m_j m_k m_l\rangle \tag{2.12}$$

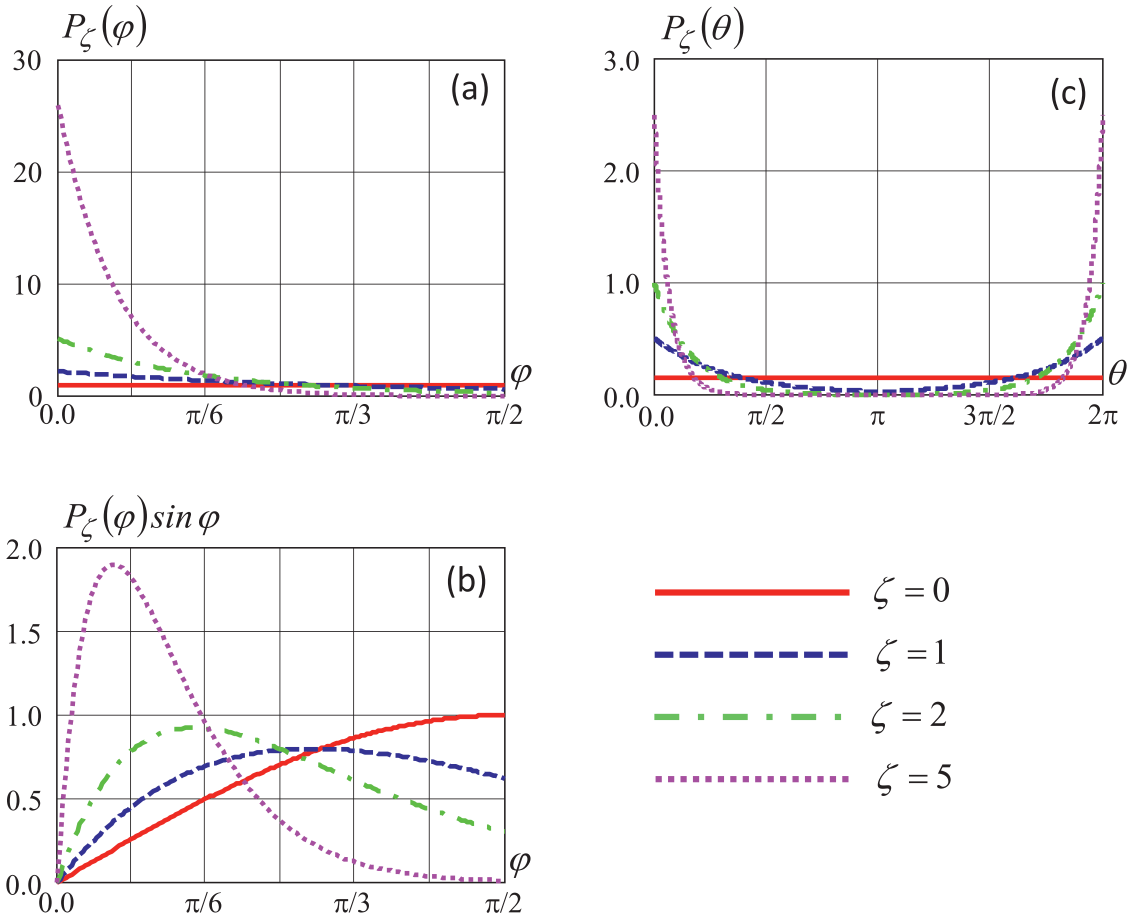

Fig. 3. (a) Dependence of the orientation distribution function P_ζ on angle φ at several values of ζ; (b) dependence of $P_\zeta \sin\varphi$ on angle φ; (c) dependence of the orientation distribution function P_ζ on angle θ.

where components of the unit vector along a fiber in the spherical coordinate system are given by Eq. (2.9). This operation is equivalent to the averaging of basic tensors $\boldsymbol{T}^{(i)}$ given by Eq. (A.1) (in the Appendix) and then dividing the result by the orientation of vectors $\boldsymbol{m}^{(p)}$. In particular, if the orientation distribution with respect to θ is approximately random (i.e., the parameter ζ_θ is sufficiently large):

$$\begin{aligned}\langle \boldsymbol{mm}\rangle &= g_1(\zeta)\boldsymbol{\theta} + g_2(\zeta)\boldsymbol{e_i e_i} \\ \langle \boldsymbol{mmmm}\rangle &= g_3(\zeta)\left(\boldsymbol{T}^{(1)} + \boldsymbol{T}^{(2)}\right) + g_4(\zeta)\left(\boldsymbol{T}^{(3)} + \boldsymbol{T}^{(4)} + \boldsymbol{T}^{(5)}\right) + g_5(\zeta)\boldsymbol{T}^{(6)}\end{aligned} \tag{2.13}$$

where $\theta_{ij} = \delta_{ij} - m_i m_j$ and:

$$g_1(\zeta) = \frac{18 - \zeta\left(\zeta^2+3\right)e^{-\zeta\pi/2}}{6\left(\zeta^2+9\right)}; \quad g_2(\zeta) = \frac{3\left(\zeta^2+3\right) + \zeta\left(\zeta^2+3\right)e^{-\zeta\pi/2}}{3\left(\zeta^2+9\right)} \tag{2.14}$$

$$\begin{aligned} g_3(\zeta) &= \frac{30}{\left(\zeta^2+9\right)\left(\zeta^2+25\right)} - \zeta e^{-\zeta\pi/2}\left[\frac{1\left(\zeta^4+30\zeta^2+149\right)}{4\left(\zeta^2+9\right)\left(\zeta^2+25\right)} - \frac{2}{15}\right] \\ g_4(\zeta) &= \frac{3\zeta^2}{\left(\zeta^2+9\right)\left(\zeta^2+25\right)} + \zeta e^{-\zeta\pi/2}\left[\frac{\zeta^4+22\zeta^2+45}{8\left(\zeta^2+9\right)\left(\zeta^2+25\right)}\right] \\ g_5(\zeta) &= \frac{\zeta^2\left(\zeta^2+7\right)}{\left(\zeta^2+9\right)\left(\zeta^2+25\right)} - \zeta e^{-\zeta\pi/2}\left[\frac{\zeta^4+10\zeta^2-15}{4\left(\zeta^2+9\right)\left(\zeta^2+25\right)}\right] \end{aligned} \tag{2.15}$$

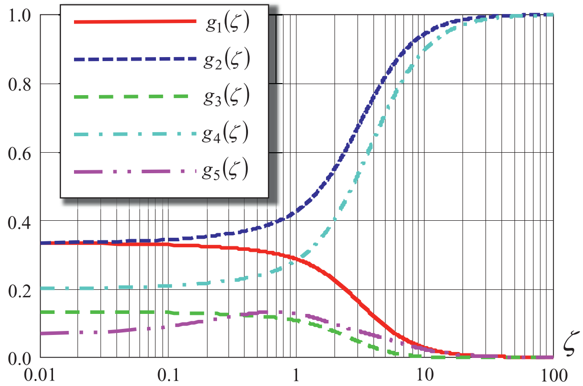

Fig. 4. Dependence of functions $g_i(\zeta)$ on the scatter parameter.

and the components of the tensor bases $\boldsymbol{T}^{(i)}$ are given in the Appendix by Eq. (A.1). Functions $g_i(\zeta)$ are shown in Fig. 4. The resulting average orientation tensor is, thus:

$$\langle \boldsymbol{H} \rangle = \sum_{k=1}^{6} h_k^* \boldsymbol{T}^{(k)} \tag{2.16}$$

and is transversely isotropic with the symmetry axis x_3 and characterized by the following coefficients:

$$\begin{aligned}
&h_1^* = h_1 + g_1(\zeta)\left[h_3 + h_4 + \frac{1}{2}h_5\right] + g_3(\zeta)\, h_6;\; h_2^* = h_2 + g_1(\zeta)\, h_5 + g_3(\zeta)\, h_6;\\
&h_3^* = g_2(\zeta)(h_3 + h_4) + g_4(\zeta)\, h_6;\; h_4^* = h_3^*\\
&h_5^* = g_2(\zeta)\, h_5 + g_4(\zeta)\, h_6;\; h_6^* = g_5(\zeta)\, h_6
\end{aligned} \tag{2.17}$$

where h_i are calculated using Eq. (A.15) in the Appendix. Similar formulas can also be written for the tensor $\langle \boldsymbol{N} \rangle$.

In the isotropic case of the inhomogeneities randomly oriented in-space:

$$\left\langle m_i m_j \right\rangle = \frac{1}{3}\delta_{ij};\; \left\langle m_i m_j m_k m_l \right\rangle = \frac{1}{15}\left(\delta_{ij}\delta_{kl} + \delta_{ik}\delta_{jl} + \delta_{il}\delta_{jk}\right) \tag{2.18}$$

so that:

$$\begin{aligned}
&h_1^* = \frac{1}{30}(14h_1 + 2h_2 + 6h_3 + 6h_4 + h_5 + 4h_6);\\
&h_2^* = \frac{1}{30}(4h_1 + 12h_2 - 4h_3 - 4h_4 + 6h_5 + 4h_6)\\
&h_3^* = h_4^* = \frac{1}{30}(12h_1 - 4h_2 + 8h_3 + 8h_4 - 2h_5 + 2h_6)\\
&h_5^* = \frac{1}{30}(8h_1 + 24h_2 - 8h_3 - 8h_4 + 12h_5 + 8h_6);\\
&h_6^* = \frac{1}{30}(16h_1 + 8h_2 + 4h_3 + 4h_4 + 4h_5 + 6h_6)
\end{aligned} \tag{2.19}$$

In the transversely-isotropic case of the inhomogeneities randomly oriented in-plane:

$$\begin{aligned}
&\left\langle m_i m_j \right\rangle = \frac{1}{2}\theta_{ij};\\
&\left\langle m_i m_j m_k m_l \right\rangle = \frac{1}{8}\left(\theta_{ij}\theta_{kl} + \theta_{ik}\theta_{jl} + \theta_{il}\theta_{jk}\right) = \frac{1}{4}\left(\boldsymbol{T}^{(1)} + \boldsymbol{T}^{(2)}\right)
\end{aligned} \tag{2.20}$$

and

$$\begin{aligned}
&h_1^* = \frac{1}{8}(2h_1 + h_2 + 6h_3 + 6h_4 + 2h_5 + 2h_6);\; h_2^* = \frac{1}{8}(2h_1 - 7h_2 - 2h_3 - 2h_4 + 2h_5 + 2h_6)\\
&h_3^* = \frac{1}{2}(h_1 + 2h_4);\; h_4^* = \frac{1}{2}(h_1 + 2h_3);\; h_5^* = h_5;\; h_6^* = \frac{1}{2}(2h_1 + h_2)
\end{aligned} \tag{2.21}$$

(see Mishurova, Cabeza, Bruno, and Sevostianov (2016) for further details)

Finally, one can write the following formulas for the effective elastic compliances of a short fiber-reinforced composite (with orientation distribution of the fibers given by Eq. (2.13)) in the framework of a non-interaction approximation:

$$s_1 = \frac{1-\nu_0}{4\mu_0(1+\nu_0)} + ch_1^*;\; s_2 = \frac{1}{2\mu_0} + ch_2^*;\; s_3 = \frac{-\nu_0}{2\mu_0(1+\nu_0)} + ch_3^*;\; s_4 = s_3$$

$$s_5 = \frac{1}{\mu_0} + ch_5^*; \quad s_6 = \frac{1}{2\mu_0(1+\nu_0)} + ch_6^* \tag{2.22}$$

where μ_0 and ν_0 are the shear modulus and Poisson's ratio of the matrix.

Interaction between the inhomogeneities can be accounted for via remote deviation of the stress field acting on the inhomogeneities. In micromechanics, such a technique is called an "effective field method" . Below, two approaches that describe this deviation are discussed.

2.2.1. Mori–Tanaka–Benveniste scheme

This scheme, proposed by Mori and Tanaka (1973) and clarified by Benveniste (1987), assumes that each inhomogeneity, treated as isolated, is placed into a uniform field that is equal to its average over the matrix phase, and generally differs from the remotely applied field. The effective properties are calculated from the non-interaction approximation, by replacing the remotely applied field by the mentioned average one. The tensor of effective elastic compliances can be expressed in terms of the compliance contribution tensors $\boldsymbol{H}_i$ of inhomogeneities as follows (see, for example, Sevostianov and Kachanov (2013)):

$$\boldsymbol{S}^{eff} = \boldsymbol{S}^0 + \left[\frac{1}{V}\sum_i V_i \boldsymbol{H}^i\right] : \left[\frac{1}{V}\sum_i V_i \left(\boldsymbol{S}^i - \boldsymbol{S}^0\right)^{-1} : \boldsymbol{H}^i + (1-c)\boldsymbol{J}\right]^{-1} \tag{2.23}$$

Replacing the summation by averaging over orientations, in the case of the inhomogeneities of the same shape having the same elastic properties, yields:

$$\boldsymbol{S}^{eff} = \boldsymbol{S}^0 + \left[\left(\boldsymbol{S}^1 - \boldsymbol{S}^0\right)^{-1} + \frac{(1-c)}{c}\langle \boldsymbol{H}\rangle^{-1}\right]^{-1} \tag{2.24}$$

In effect, the effective elastic properties are expressed in terms of tensor $\langle \boldsymbol{H}\rangle$ given by Eqs. (2.16) and (2.17).

2.2.2. Maxwell scheme

The Maxwell homogenization scheme (Maxwell, 1873) can also be considered as a variant of the effective field method (Sevostianov & Kachanov, 2014). Sevostianov and Giraud (2013) and Sevostianov (2014) reformulated Maxwell's scheme for the general case of a composite with arbitrary orientation distribution of inhomogeneities of diverse shape using property contribution tensors. They suggested that the domain Ω of the volume V^* be cut from a composite and placed into the matrix material. The effect produced by this element is described either by the sum of compliance contribution tensors of the inhomogeneities $\frac{1}{V}\sum_i V_i \boldsymbol{H_i}$ or by the compliance contribution tensor $\boldsymbol{H}_{eff}$ of the entire domain considered as an individual inhomogeneity with homogenized unknown properties. Equating these two quantities, the general equation for the Maxwell scheme can be obtained from:

$$\frac{V^*}{V}\boldsymbol{H_{eff}} = \frac{1}{V}\sum_i V_i \boldsymbol{H_i} \tag{2.25}$$

Variables within the right side of the Eq. (2.25) are known. The left side of this equation reflects the combined effect of the overall properties of the material on Ω and its shape. According to Eq. (2.5), for an ellipsoidal shape of Ω, equation Eq. (2.19) yields:

$$\boldsymbol{S_{eff}} = \boldsymbol{S_0} + \left\{\left[\frac{1}{V}\sum_i V_i {\boldsymbol{H}_{eff}}^i\right]^{-1} - \boldsymbol{Q}_\Omega\right\}^{-1} \tag{2.26}$$

where $\boldsymbol{Q}_\Omega$ reflects the effect of the shape of Ω and has to be calculated using Eq. (A.12) in the Appendix. Replacing the summation by averaging over orientations yields:

$$\boldsymbol{S_{eff}} = \boldsymbol{S_0} + c\left\{\langle \boldsymbol{H}\rangle^{-1} - c\boldsymbol{Q}_\Omega\right\}^{-1} \tag{2.27}$$

Thus, the effective elastic properties are again expressed in terms of the tensor $\langle \boldsymbol{H}\rangle$.

The key parameter required for calculation of the components of this tensor is the orientation scatter parameter ζ entered into Eq. (2.15) as the argument of functions $g_i(\zeta)$. This parameter can be evaluated experimentally using CT-based methods. In the next section, the applicability of CT methodology will be shown for extraction of information about the ODF of an example polymer-fiber reinforced concrete.

3. Experimental

3.1. Preparation of specimens

The cement-mortar prism with size 40 × 40 × 160 mm have been produced (Fig. 5a). It consisted of Portland cement (CEM I 32.5 R), ground limestone, silica sand, water and polyacrylonitrile (PAN) fibers. The volume fraction of cement and

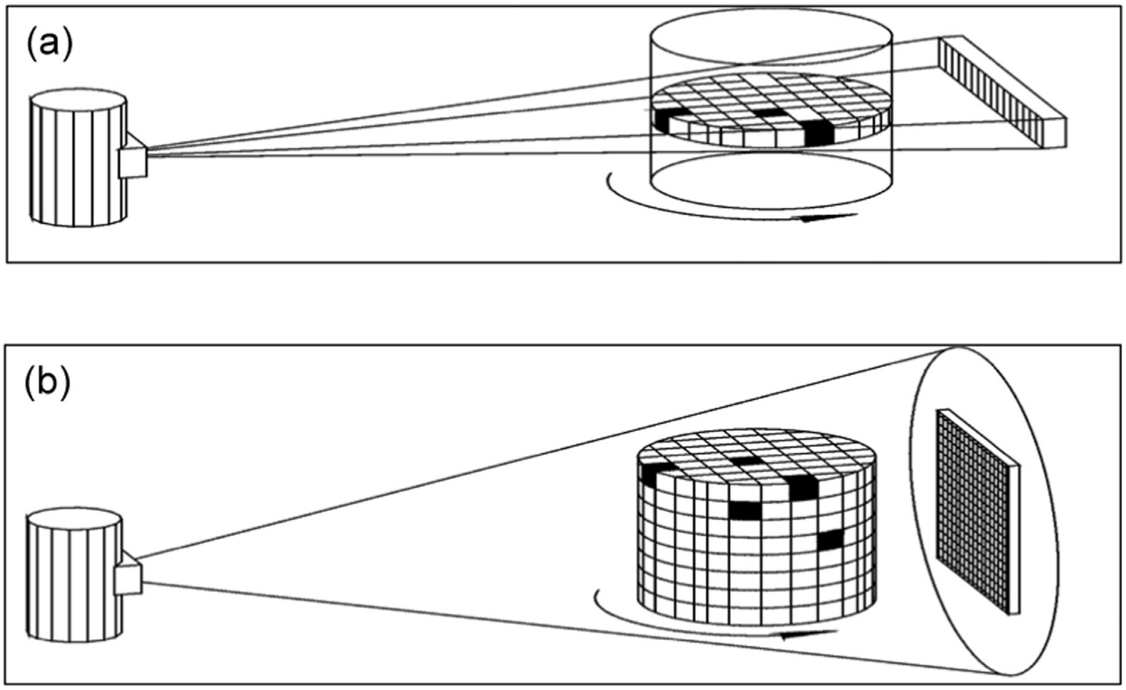

Fig. 5. (a) Concrete specimens used in mechanical tests; (b) specimens used for CT experiments.

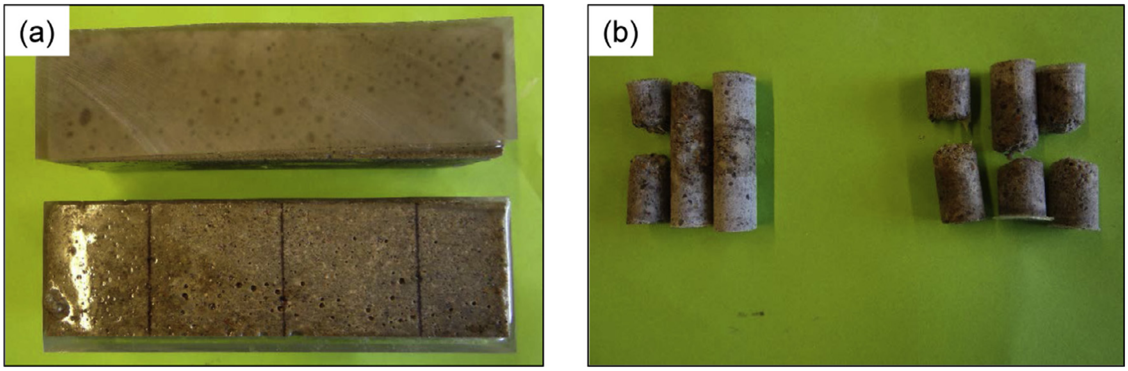

Fig. 6. Schematic diagram of the CT: (a) conventional system - tomograms are measured slice by slice, and the sample is not only rotated, but also translated perpendicular to the plane of the scanning slices; (b) 3D CT - the detector panel no longer consists of a row of detector elements but of a square field with an array of detector elements.

limestone/sand in mixture was 30% and 70%, respectively. PAN fibers had a diameter of 15 µm and length of 4 mm. The volume fraction of fibers in the material was 0.5%. The preparation of mortar prisms was performed according to DIN EN 196-1. A conventional mortar mixer was used. After mixing, test specimens were compacted by using a vibrating table and placed into a container with water for 24 h. Then, all specimens were stored for 6 days under water with a temperature of 20 °C.

Cylindrical specimens with length of 40 mm and diameter of 10 mm were then drilled from a mortar prism for CT measurements (Fig. 5b,c). Before drilling, the prism was impregnated with epoxy resin in order to prevent disintegration of the sample.

3.2. Computed tomography

During CT experiments, the linear absorption coefficient of the material in each point of the region of interest in the specimen is measured. The coefficient is dependent on the incident X-ray energy and on the atomic number of the material. In most cases it can be regarded as linear, correlating to the specific density. In conventional systems, tomograms are measured slice by slice, and the sample is not only rotated, but also translated perpendicular to the plane of the scanning slices (Fig. 6a). In more advanced types of tomography equipment, the object to be measured is moved constantly, allowing

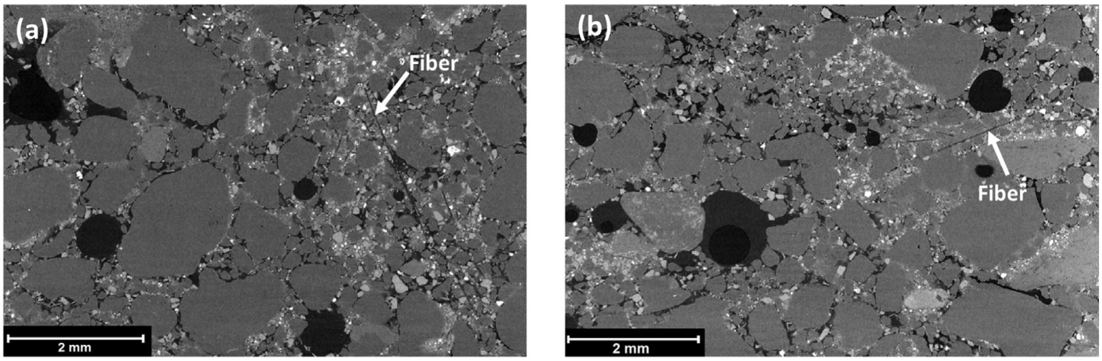

2D reconstructed slices from CT measurements (a) in plane X1X3 and (b) in plane X2X3

Fig. 7. 2D reconstructed slices from CT measurements (a) in plane X_1X_3 and (b) in plane X_2X_3.

the slices to generate a continuous volume. Measuring 2D slices enables the use of more efficient detectors and limits the number of image artifacts due to scattered radiation from the object.

In the case of 3D CT, the detector no longer consists of a row of detector elements but of a square field with an array of detector elements (Fig. 6b). The detector measures conventional radiological images. Upon turning the object and acquiring a radiograph at each angle, a complete data set is collected within one turn. Computer programs are available to reconstruct the 3D volume from the radiographs. Resolutions in the micrometer range are achieved either by a high resolution detector (small pixel size, down to 0.2 µm) and a parallel beam source (e.g., with synchrotron radiation), or by a cone-shaped X-ray beam with a focal spot in the micro-meter range and a coarse but efficient detector. In this case, the cone-beam geometry is exploited through the use of a magnification apparatus.

High X-ray penetration depths can be achieved through the use of higher acceleration voltages, which at the present time are capable of reaching 12MeV. Through the use of such high voltages, CT reconstructions can be created for samples made from materials as dense as iron with a thickness of up to 400 mm. The disadvantage of using such high voltages is the corresponding effect on the minimum achievable focal spot size, which for high-energy devices is in the range of 1 mm. Such a large focal spot size is insufficient for high-resolution CT reconstructions since the resolution of CT images becomes coarser with increasing focal spot size. Standard X-ray tubes fill the gap between synchrotron sources and high-energy devices. They possess beam focal spot sizes in the range of a few micrometers, and have acceleration voltages in the range of 100–600 keV.

Although the use of the highest possible X-ray energy is generally desirable in order to investigate highly absorbing materials, it is also important to limit both the effects of X-ray scattering and to ensure adequate levels of X-ray transmission. The transmission of approximately 10–30% of the X-ray beam energy through the sample is considered to be optimal for CT (Buzug, 2008). Image artifacts from beam hardening effects can also be limited through the use of higher X-ray energies. In the case of two dimensional detectors, the effects of scattered radiation may be reduced through the use of appropriate filters. To generate images from the measured data, mathematical processes like filtered back-projection, algebraic reconstruction, or iterative computation have to be used.

The CT measurements were performed by using a v|tome|x L 300 CT scanner from General Electric. During each scan, 3000 projections were acquired at 0.12° rotation increments with the acquisition time for each projection lasting 2 seconds. An acceleration voltage of 80 keV and a tube current of 50 µA were used throughout the experiments. To obtain a better statistical sample of the orientation distribution of fibers within the concrete, six CT measurements at different locations along the sample's height were carried out, each with a spatial resolution of 6.65 µm. Examples of reconstructed slices of one of the 3D reconstructions are presented in Fig. 7.

Image analysis of the reconstructed volumes was performed using Amira ZIB Edition from the Konrad–Zuse–Zentrum Berlin (ZIB) (Stalling, Westerhof, & Hege, 2005). Due to the low contrast between the fibers and the matrix material, and because of the small fiber diameter (15 µm), identification of fibers by global segmentation was not possible. However, it was possible to trace fibers by using a template matching algorithm implemented in ZIB Amira. This tool creates correlation and orientation fields by matching the reconstructed volume with a cylindrical template, which is defined by user. This approach helps to trace fibers (and other tube-like structures) even in noisy data. In the present study, implementation of such an algorithm had some limitations. The crossing of low-density fibers with pores and aggregates, as well as damage of the fibers during sample drilling, resulted in difficulties in estimating fiber length. However, observations indicated that bending of fibers was not significant in this material. Therefore, reliable fiber orientation information could indeed be extracted even from incomplete or damaged fibers. The improper identification of material interface zones (such as the surface of aggregate particles) as fibers was minimized by introducing additional strategies, such as fiber length control.

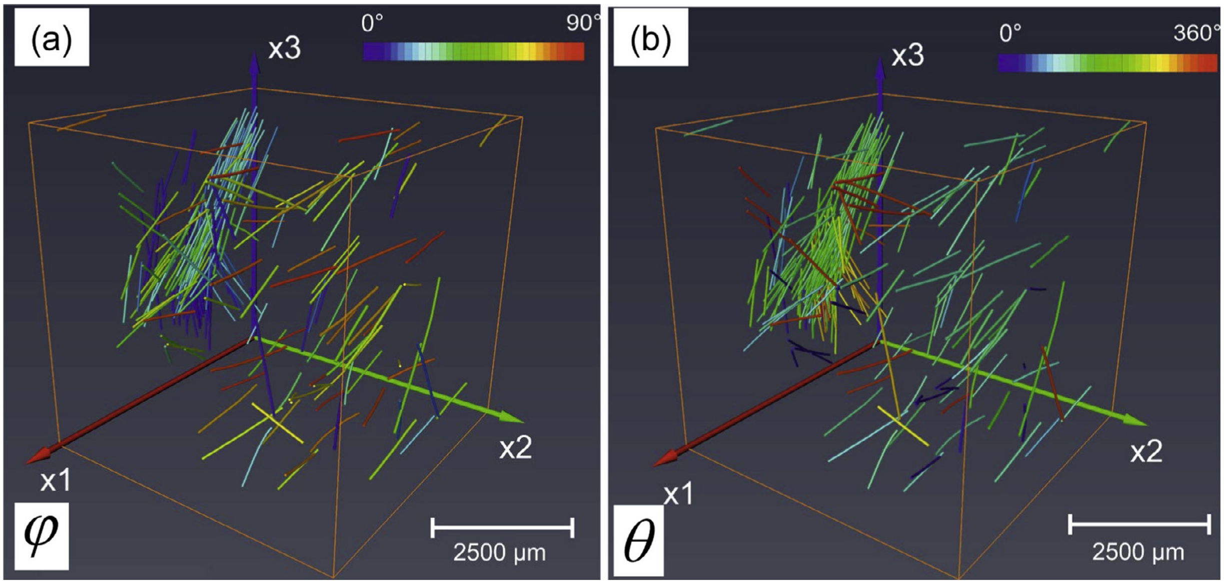

Fig. 8. Depiction of fiber orientation distribution obtained by CT measurements with respect to angles φ (a) and θ (b).

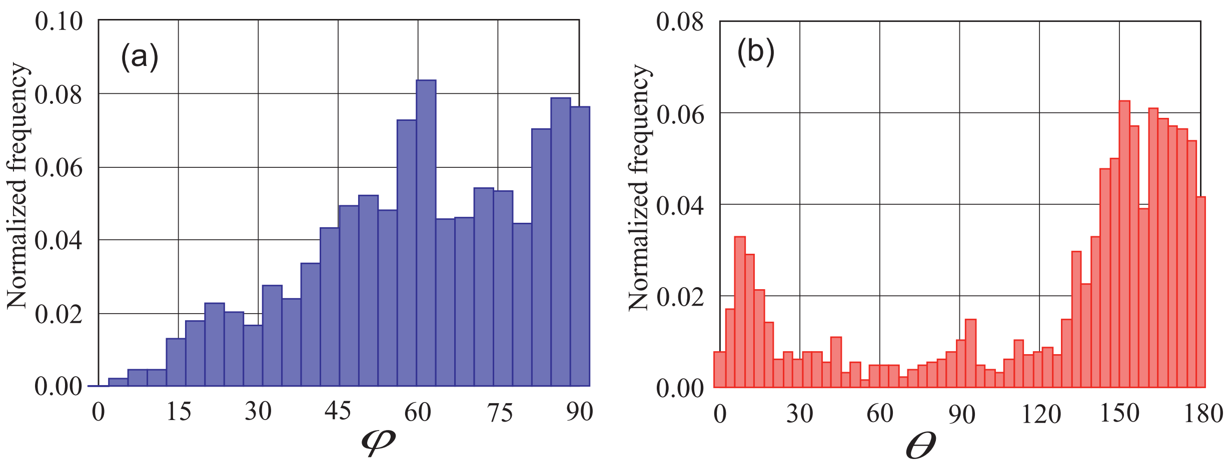

Fig. 9. Histograms of normalized frequency distribution for angles φ (a) and θ (b).

4. Results and discussion

4.1. CT reconstructions and calculation of the scatter parameter

As an output of the template matching algorithm, two orientation angles in spherical coordinates θ and φ for each fiber were obtained. Fig. 8 presents examples of fiber orientation distributions in θ and φ obtained for one CT scan. These data were used to produce orientation distribution histograms (Fig. 9) normalized by the total number of fibers measured within the scanned regions of the sample. It is to be noted that in the concrete casting process, polymer fibers are difficult to distribute with a defined orientation, due to the tendency of the fibers to agglomerate. From the orientation distribution histogram, a high number of fibers were observed to be oriented roughly parallel to the X-Z plane (θ near 0° or 180°) with an orientation angle φ larger than 45° To obtain the orientation distribution probability density, the normalized frequency has to be multiplied by $52/\pi$ (since the interval from 0 to $\pi/2$ is subdivided into 26 subintervals).

A custom MATLAB script was developed to determine the scatter parameter ζ from CT data using nonlinear least squares fitting (The Mathworks 2016). The Trust Region Reflective method was used to minimize the squared second norm of the vector $\boldsymbol{e}$ denoting the error between the distribution calculated using Eq. (2.11) and the experimental data:

$$\min_{(\zeta)} \|\boldsymbol{e}\|_2^2 = \min_{(\zeta)} \left\| \frac{P(\varphi, \zeta)\sin\alpha - P_{\exp}(\varphi)}{\bar{P}_{\exp}(\varphi)} \right\|_2^2 \tag{4.1}$$

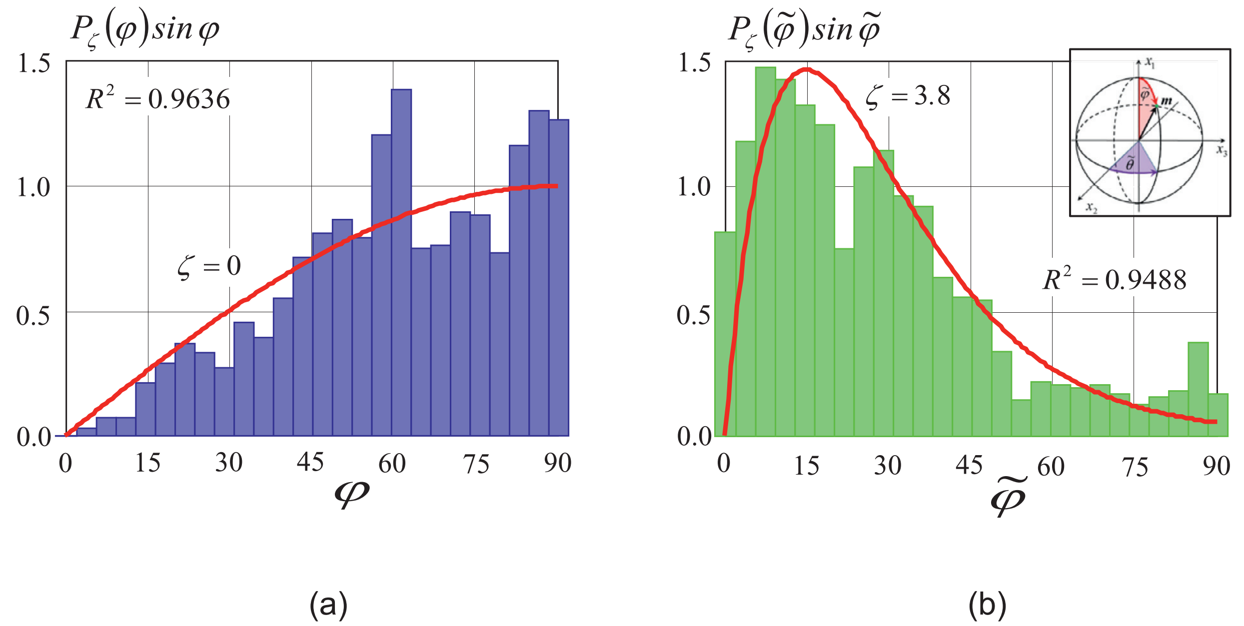

Fig. 10. (a) Orientation distribution function for angle φ and its best fit by the first equation in Eq. (2.11); (b) orientation distribution function for angle $\tilde{\varphi}$ in the coordinate system shown in the inset and its best fit by the first equation in Eq. (2.11).

Table 1
Mechanical properties of the constituents.

	Young's modulus (GPa)	Poisson's ratio
Concrete matrix	45.0	0.15
Polyacrylonitrile fibers	26.8	0.19

where $P(\varphi, \zeta)$ is the vector of probability density calculated using the first of the expressions in Eq. (2.11) for the given scatter parameter ζ and the inclination angle φ, $P_{\exp}(\varphi)$ is the vector of experimentally obtained normalized frequencies and $\bar{P}_{\exp}(\varphi)$ is the mean value of $P_{\exp}(\varphi)$. The step of variation of the scatter parameter was chosen as 0.1. Fig. 10a shows that the best fit for this step was produced by $\zeta = 0$ with $R^2 = 0.9636$. This means that the distribution with respect to angle φ is isotropic and the material properties are transversely-isotropic with respect to the isotropy plane x_2x_3 and symmetry axis x_1. We now change the coordinate system as shown in the inset of Fig. 10b, and the orientation distribution probability density was calculated with respect to angle $\tilde{\varphi}$ (Fig. 10b). Again, the expressions in Eq. (2.11) were used to calculate the vector of probability density and the best fit was produced by $\zeta = 3.8$ (red line in Fig. 10b) with $R^2 = 0.9488$. Thus, the overall distribution of the fibers is transversely-isotropic, at least in the sense of approximate symmetry (Sevostianov & Kachanov, 2007), with the x_1-axis being the axis of symmetry and with the scatter parameter $\zeta = 3.8$.

4.2. Calculation of the model elastic constants

With the fitted fiber orientation distribution function, the effective elastic properties of the composite can be calculated. Fig. 11 shows the effective engineering elastic constants calculated in the frameworks of the non-interaction approximation, Mori–Tanaka–Benveniste and Maxwell schemes for this orientation distribution (the properties of the constituents are given in Table 1). It can be observed that since the fibers have a lower Young's modulus than the concrete matrix, insertion of an increasing amount of them does soften the composite. This softening is indeed anisotropic, following the slight anisotropy of the fiber orientation distribution.

The interest of adding polymer fibers resides mainly in the increase of the damage tolerance, which is however beyond the scope of this short study.

The results from these three different frameworks showed a great degree of consistency, although the Mori–Tanaka–Benveniste scheme showed the most significant amount of deviation from the others. It is also interesting to note that neglecting interactions would not lead to large deviations from the more sophisticated Maxwell homogenization scheme.

The results of these calculations will now be validated through a mechanical testing program. A forthcoming publication is planned in which the results of the mechanical testing program will be compared to the analytical predictions provided here and corresponding conclusions will be drawn about the accuracy of the analytical methods and possible schemes for their improvement will be proposed.

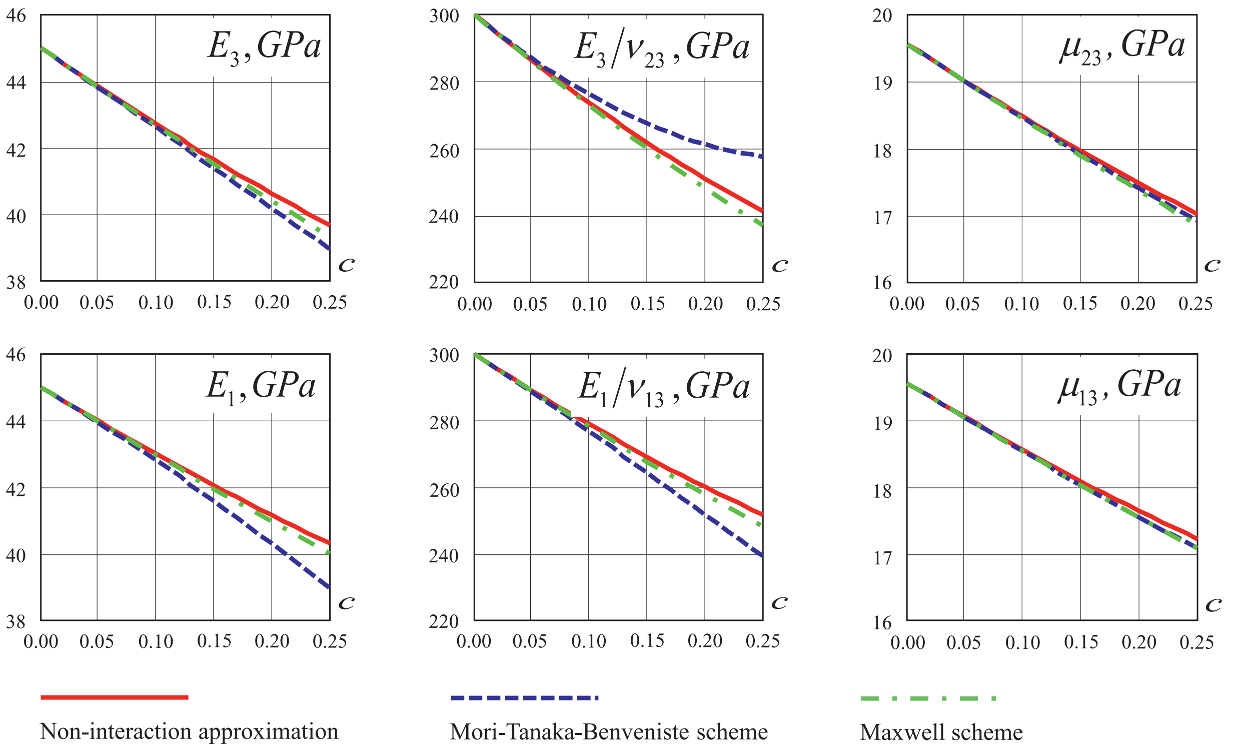

Fig. 11. Dependence of the elastic constants (in GPa) of the Polyacrylonitrile fibers reinforced concrete on the volume fraction of fibers calculated using Eq. (2.22) (non-interaction approximation), Eq. (2.24) (Mori–Tanaka–Benveniste scheme), and Eq. (2.27) (Maxwell scheme).

These calibrated and validated analytical methods will then serve as the basis for the development of numerical models of fiber-reinforced composite materials with greater accuracy in simulating the behavior of these materials in the elastic performance region. This will be useful for simulating both the behavior of fiber-reinforced composite elements prior to matrix cracking and after matrix cracking, since regions of intact material located between matrix cracks continue to exhibit elastic performance behavior.

5. Concluding remarks

In order to calculate the equivalent elastic constants of a polymer-fiber reinforced concrete composite (a transversely isotropic material), X-ray CT was used to experimentally obtain information about the orientation distribution of fibers. We showed how this experimental information can be incorporated into usual micromechanical homogenization schemes (non-interaction approximation, Mori–Tanaka–Benveniste, and Maxwell scheme), to calculate the effective engineering elastic constants for the material.

The model can be used for the prediction of the behavior of fiber-reinforced composite materials both prior to and following matrix cracking, since overall material performance after the initiation of matrix cracking is still highly dependent on the behavior of undamaged elastic material regions located between cracking zones. Finally, theoretical modeling of the elastic properties of composites with different fiber volume fractions as well as with different matrix and fiber properties would allow a speedier materials selection process. It would also facilitate the saving of costly experimental work, paramount in industrial research.

Acknowledgment

This work was supported by the National Group of Mathematical Physics GNFM-IndAM (Italy), FP7 Project TAMER IRSES-GA-2013-610547, NASA Cooperative Agreement NNX15AL51H (through NM Space Grant Consortium), grant 14.Z50.31.0036 awarded by Department of Education and Science of the Russian Federation to R. E. Alexeev Nizhny Novgorod Technical University, Bundesministerium für Bildung und Forschung (BMBF)grant 13N13306, and the BAM Visiting Scientist Grant Program. The authors are grateful to Mr. Philipp Drabetzki (BAM, Berlin) for sample preparation.

Appendix A. Tensor basis in the space of fourth rank tensors and representation of some tensors in its terms

A convenient technique will be outlined of analytic inversion and multiplication of 4th rank tensors. It is based on expressing tensors in "standard" tensor bases as suggested by Kunin (1983) and Walpole (1984). In the case of the transversely isotropic elastic symmetry, the following basis is most convenient:

$$\begin{aligned}&T^{(1)}_{ijkl}=\theta_{ij}\theta_{kl};\ T^{(2)}_{ijkl}=\left(\theta_{ik}\theta_{lj}+\theta_{il}\theta_{kj}-\theta_{ij}\theta_{kl}\right)/2;\ T^{(3)}_{ijkl}=\theta_{ij}m_km_l;\\&T^{(4)}_{ijkl}=m_im_j\theta_{kl};\ T^{(5)}_{ijkl}=\left(\theta_{ik}m_lm_j+\theta_{il}m_km_j+\theta_{jk}m_lm_i+\theta_{jl}m_km_i\right)/4;\\&T^{(6)}_{ijkl}=m_im_jm_km_l\end{aligned}\tag{A.1}$$

where $\theta_{ij}=\delta_{ij}-m_im_j$ and $\boldsymbol{m}=m_1\boldsymbol{e}_1+m_2\boldsymbol{e}_2+m_3\boldsymbol{e}_3$ is a unit vector along the axis of transverse symmetry.

These tensors form the closed algebra with respect to the operation of (non-commutative) multiplication (contraction over two indices):

$$\left(\boldsymbol{T}^{(\alpha)}:\boldsymbol{T}^{(\beta)}\right)_{ijkl}\equiv T^{(\alpha)}_{ijpq}T^{(\beta)}_{pqkl}\tag{A.2}$$

The inverse of any fourth rank tensor $\boldsymbol{X}$, as well as the product $\boldsymbol{X}:\boldsymbol{Y}$ of two such tensors, is readily found in the closed form, as soon as the representations in the basis:

$$\boldsymbol{X}=\sum_{k=1}^{6}X_k\boldsymbol{T}^{(k)};\ \boldsymbol{Y}=\sum_{k=1}^{6}Y_k\boldsymbol{T}^{(k)}\tag{A.3}$$

are established. Indeed:

a) inverse tensor $\boldsymbol{X}^{-1}$ defined by $X^{-1}_{ijmn}X_{mnkl}=(X_{ijmn}X^{-1}_{mnkl})\ =J_{ijkl}$ is given by

$$\boldsymbol{X}^{-1}=\frac{X_6}{2\Delta}\boldsymbol{T}^{(1)}+\frac{1}{X_2}\boldsymbol{T}^{(2)}-\frac{X_3}{\Delta}\boldsymbol{T}^{(3)}-\frac{X_4}{\Delta}\boldsymbol{T}^{(4)}+\frac{4}{X_5}\boldsymbol{T}^{(5)}+\frac{2X_1}{\Delta}\boldsymbol{T}^{(6)}\tag{A.4}$$

where $\Delta=2(X_1X_6-X_3X_4)$.

b) the product of two tensors $\boldsymbol{X}:\boldsymbol{Y}$ (tensor with $ijkl$ components equal to $X_{ijmn}Y_{mnkl}$) is given by:

$$\begin{aligned}\boldsymbol{X}:\boldsymbol{Y}=&(2X_1Y_1+X_3Y_4)\boldsymbol{T}^{(1)}+X_2Y_2\boldsymbol{T}^{(2)}+(2X_1Y_3+X_3Y_6)\boldsymbol{T}^{(3)}\\&+(2X_4Y_1+X_6Y_4)\boldsymbol{T}^{(4)}+\frac{1}{2}X_5Y_5\boldsymbol{T}^{(5)}+(X_6Y_6+2X_4Y_3)\boldsymbol{T}^{(6)}\end{aligned}\tag{A.5}$$

If x_3 is the axis of transverse symmetry, the general transversely isotropic fourth-rank tensor, being represented in this basis:

$$\Psi_{ijkl}=\sum\psi_mT^m_{ijkl}\tag{A.6}$$

has the following components:

$$\begin{aligned}&\psi_1=(\psi_{1111}+\psi_{1122})/2;\ \psi_2=2\psi_{1212};\ \psi_3=\psi_{1133};\ \psi_4=\psi_{3311};\\&\psi_5=4\psi_{1313};\ \psi_6=\psi_{3333}\end{aligned}\tag{A.7}$$

Utilizing Eq. (A.7), one obtains the following representations:

- The tensor of elastic compliances of an isotropic material $S_{ijkl}=\sum s_mT^m_{ijkl}$ has the following components:

$$s_1=\frac{1-\nu}{4\mu(1+\nu)};\ s_2=\frac{1}{2\mu};\ s_3=s_4=\frac{-\nu}{2\mu(1+\nu)};\ s_5=\frac{1}{\mu};\ s_6=\frac{1}{2\mu(1+\nu)}.\tag{A.8}$$

- The tensor of elastic stiffness of an isotropic material by $C_{ijkl}=\sum c_mT^m_{ijkl}$ has components:

$$c_1=\lambda+\mu;\ c_2=2\mu;\ c_3=c_4=\lambda;\ c_5=4\mu;\ c_6=\lambda+2\mu.\tag{A.9}$$

where $\lambda=2\mu\nu/(1-2\nu)$.

- Unit fourth rank tensors are represented in the form:

$$J^{(1)}_{ijkl}=\left(\delta_{ik}\delta_{lj}+\delta_{il}\delta_{kj}\right)/2=\frac{1}{2}T^1_{ijkl}+T^2_{ijkl}+2T^5_{ijkl}+T^6_{ijkl}\tag{A.10}$$

$$J^{(2)}_{ijkl}=\delta_{ij}\delta_{kl}=T^1_{ijkl}+T^3_{ijkl}+T^4_{ijkl}+T^6_{ijkl}\tag{A.11}$$

- Tensor $\boldsymbol{Q}$, defined by Eq. (2.6), in the case of a spheroidal inhomogeneity ($a_1=a_2=a$) of the aspect ratio $\gamma=a/a_3$, has the following components (see, for example, Sevostianov and Kachanov (2002)):

$$q_1=\mu[4\kappa-1-2(3\kappa-1)f_0-2\kappa f_1];\ q_2=2\mu[1-(2-\kappa)f_0-\kappa f_1];$$

$$q_3 = q_4 = 2\mu[(2\kappa - 1)f_0 + 2\kappa f_1]; \quad q_5 = 4\mu(f_0 + 4\kappa f_1);$$
$$q_6 = 8\mu(\kappa f_0 - \kappa f_1) \tag{A.12}$$

where $\kappa = 1/[2(1-\nu)]$ and functions f_0 and f_1 are given by:

$$f_0 = \frac{1-g}{2\left(1-\gamma^2\right)}; f_1 = \frac{1}{4\left(1-\gamma^2\right)^2}\left[\left(2+\gamma^2\right)g - 3\gamma^2\right] \tag{A.13}$$

where:

$$g(\gamma) = \begin{cases} \frac{\gamma^2}{\sqrt{\gamma^2-1}} arctan\sqrt{\gamma^2-1}, & oblate\ spheroid,\ \gamma \geq 1 \\ \frac{\gamma^2}{2\sqrt{1-\gamma^2}} ln\frac{1+\sqrt{1-\gamma^2}}{1-\sqrt{1-\gamma^2}}, & prolate\ spheroid,\ \gamma \leq 1 \end{cases} \tag{A.14}$$

Factors entering the representation of the compliance contribution tensor $\boldsymbol{H}$ of the spheroidal inhomogeneity with bulk and shear moduli K_1 and μ_1 embedded in the matrix with elastic constants K_0 and μ_0 in terms of the tensor basis are given by (Sevostianov & Kachanov, 1999; 2002):

$$h_1 = \frac{1}{2\Delta}\left[K + \frac{4}{3}\mu + q_6\right]; h_2 = \frac{1}{2\mu + q_2}; h_3 = h_4 = -\frac{1}{\Delta}\left[K - \frac{2}{3}\mu + q_3\right];$$
$$h_5 = \frac{4}{4\mu + q_5}; h_6 = \frac{2}{\Delta}\left[K + \frac{1}{3}\mu + q_1\right] \tag{A.15}$$

where K and μ are defined by Eq. (2.15) and

$$\Delta_H = 2\left[3\mu K + K(q_1 + q_6 - 2q_3) + \frac{\mu}{3}(4q_1 + q_6 + 4q_3) + \left(q_1 q_6 - q_3^2\right)\right] \tag{A.16}$$

References

Arenhart, R. G., Barra, G. M. O., & Fernandes, C. P. (2015). Simulation of percolation threshold and electrical conductivity in composites filled with conductive particles: Effect of polydisperse particle size distribution. *Polymer Composites* in press:12 August. doi:10.1002/pc.23155.

Barnett, S. J., Lataste, J. F., Parry, T., Millard, S. G., & Soutsos, M. N. (2010). Assessment of fibre orientation in ultra high performance fibre reinforced concrete and its effect on flexural strength. *Materials and Structures, 43*, 1009–1023.

Bay, R. S., & Tucker, C. L. (1992). Stereological measurement and error estimates for three-dimensional fiber orientation. *Polymer Engineering and Science, 32*(4), 240–253.

Blanco, A. (2013). *Characterization and modelling of SFRC elements* Doctoral Thesis. Barcelona: Universitat Politècnica de Catalunya.

Benveniste, Y. (1987). A new approach to the application of Mori–Tanaka's theory in composite material. *Mechanics of Materials, 6*, 147–157.

Bernasconi, A., Cosmi, F., & Hine, P. J. (2012). Analysis of fibre orientation distribution in short fibre reinforced polymers: A comparison between optical and tomographic methods. *Composites Science and Technology, 72*, 2002–2008.

Bruno, G., & Fernandez, R. (2007). The dependence of the Eshelby model predictions on the microstructure of metal matrix composites. *Acta Materialia, 55*(4(February)), 1267–1274.

Buzug, T. M. (2008). *Computed tomography- from photon statistics to modern cone-beam CT*. Berlin/Heidelberg: Springer Verlag.

Chen, C. H., & Wang, Y. C. (1996). Effective thermal conductivity of misoriented shortfiber reinforced thermoplastics. *Mechanics of Materials, 23*(3), 217–228.

Chen, T., Dvorak, G. J., & Benveniste, Y. (1992). Mori–Tanaka estimates of the overall elastic moduli of certain composite materials. *Journal of Applied Mechanics, 59*(3), 539–546.

Chou, T. W., & Nomura, S. (1980-81). Fibre orientation effects on the thermoelastic properties of short-fiber composites. *Fibre science & technology, 14*, 279.

Clarke, A., & Eberhardt, C. (1999). The representation of reinforcing fibres in composites as 3D space curves. *Composites Science and Technology, 59*, 1227–1237.

Cusatis, G., & Nakamura, H. (2011). "Discrete modeling of concrete materials,". Preface to the Special Issue on Discrete Models. *Cement and Concrete Composites, 33*, 865–866.

Cusatis, G., Pelessone, D., & Mencarelli, A. (2011). Lattice discrete particle model (LDPM) for failure behavior of concrete I: Theory. *Cement and Concrete Composites, 33*, 881–890.

di Prisco, M., Ferrara, L., & Lamperti, M. G. L. (2013). Double edge wedge splitting (DEWS): An indirect tension test to identify post-cracking behaviour of fibre reinforced cementitious composites. *Materials and Structures, 46*, 1893–1918.

DIN EN 196-1: Methods of testing cement – Part 1: Determination of strength.

Dunn, M. L., Ledbetter, H., Heyliger, P. L., & Choi, C. S. (1996). Elastic constants of textured short-fiber composites. *Journal of the Mechanics and Physics of Solids, 44*, 1509–1541.

Dunn, M. L., & Ledbetter, H. (1997). Elastic–plastic behavior of textured short fiber composites. *Acta Materialia, 45*(8), 3327–3340.

Dunn, M. L., & Ledbetter, H. (2000). Micromechanically-based acoustic characterization of the fiber orientation distribution function of morphologically textured short-fiber composites: Prediction of thermomechanical and physical properties. *Material Science and Engineering, A285*, 56–61.

Duschlbauer, D., Bohm, H., & Pettermann, H. (2003). Numerical simulation of thermal conductivity of MMCs: Efect of thermal interface resistance. *Materials Science & Technology, 19*(8), 1107–1114.

Eberhardt, C., & Clarke, A. (2001). Fibre-orientation measurements in short-glass-fibre composites. Part I: Automated, high angular- resolution measurement by confocal microscopy. *Composites Science and Technology, 61*, 1389–1400.

Fernandez Serrano, R., Bruno, G., & Gonzalez-Doncel, G. (2004). Correlation between residual stresses and the strength differential effect in PM 6061Al–15 vol% SiC_w composites: Experiments, models and predictions. *Acta Materialia, 52*(19(November)), 5471–5483.

Ferrari, M. (1991). Asymmetry and the high concentration limit of the Mori–Tanaka effective medium theory. *Mechanics of Materials, 11*(3), 251–256.

Ferrara, L., & Meda, A. (2006). Relationships between fibre distribution, workability and mechanical properties of SFRC applied to precast roof elements. *Materials and Structures, 39*, 411–420.

Ferrari, M., & Johnson, M. C. (1989). Effective elasticities of short-fiber composites with arbitrary orientation distribution. *Mechanics of Materials, 8*(1), 67–73.

Ferrari, M., & Marzari, N. (1992). A Mori–Tanaka theory for textured short-fiber composites: Application. *Journal of Energy Resources Technology, 114*(2), 101–104.

Fu, S. &, & Lauke, B. (1998). The elastic modulus of misaligned short-fiber-reinforced polymers. *Composites Science and Technology, 58*(3-4), 389–400.

Hashin, Z. (1983). Analysis of composite materials –a survey. *Journal of Applied Mechanics, 50*, 481–505.

Hill, R. (1965). A self-consistent mechanics of composite materials. *Journal of the Mechanics and Physics of Solids, 13*(4), 213–222.
Horii, H., & Nemat-Nasser, S. (1983). Overall moduli of solids with microcracks: Load-induced anisotropy. *Journal of the Mechanics and Physics of Solids, 31*, 155–171.
Kachanov, M., Tsukrov, I., & Shafiro, B. (1994). Effective properties of solids with randomly located defects. In D. Breusse (Ed.), *Probabilities and Materials: Tests, Models and Applications* (pp. 225–240). Kluwer Publ..
Kachanov, M., & Sevostianov, I. (2005). On quantitative characterization of microstructures and effective properties. *International Journal of Solids and Structures, 42*, 309–336.
Kang, G., Yang, C., & Zhang, J. (2002). Tensile properties of randomly oriented short δ-Al2O3 fiber reinforced aluminum alloy composites. I. Microstructure characteristics, fracture mechanisms and strength prediction. *Composites-A, 33*, 647–656.
Kang, S. T., Lee, B. Y., Kimc, J.-K., & Kim, Y. Y. (2011). The effect of fibre distribution characteristics on the flexural strength of steel fibre-reinforced ultra high strength concrete. *Construction and Building Materials, 25*(5), 2450–2457.
Kang, S.-T., & Kim, J.-K. (2012). Investigation on the flexural behavior of UHPCC considering the effect of fiber orientation distribution. *Construction and Building Materials, 28*, 57–65.
Kunin, I. A. (1983). *Elastic media with microstructure*. Berlin: Springer Verlag.
Lataste, J. F., Behloul, M., & Breysse, D. (2008). Characterization of fibres distribution in a steel fibre reinforced concrete with electrical resistivity measurements. *NDT and E International, 41*(8), 638–647.
Lee, B. Y., Kim, J.-K., Kim, J.-S., & Kim, Y. Y. (2009). Quantitative evaluation technique of PVA (Polyvinyl Alcohol) fiber dispersion in engineered cementitious composites. *Cement & Concrete Composites, 31*(6), 408–417.
Li, S. (2000). General unit cells for micromechanical analyses of unidirectional composites. *Composites Part A, 32*, 815–826.
Liu, J., Li, C., Liu, J., Cui, G., & Yang, Z. (2013). Study on 3D spatial distribution of steel fibers in fiber reinforced cementitious composites through micro-CT technique. *Construction and Building Materials, 48*, 656–661.
Lu, Y., & Liaw, P. K. (1995). Effect of particle orientation in silicon-carbide particule-reiforced aluminium-matrix composite extrusions on ultrasonic velocity-measurements. *Journal of composite materials, 29*(8), 1096–1116.
Maxwell, J. C. (1873). *A treatise on electricity and magnetism*. Oxford: Clarendon Press.
Mishurova, T., Cabeza, S., Bruno, G., & Sevostianov, I. (2016). Average phase stress concentrations in multiphase metal matrix composites under compressive loading. *International Journal of Engineering Science, 106*, 245–261.
Mori, T., & Tanaka, K. (1973). Average stress in matrix and average elastic energy of materials with misfitting inclusions. *Acta Metallurgica, 21*, 571–574.
Nemat-Nasser, S., & Hori, M. (1993). *Micromechanics: Overall properties of heterogeneous solids*. Amsterdam: Elsevier.
Oesch, T. (2015). *Investigation of Fiber and Cracking Behavior for Conventional and Ultra-High Performance Concretes using X-Ray Computed Tomography*. Urbana, IL: University of Illinois at Urbana-Champaign.
Pérez, R., Banda, S., & Ounaies, Z. (2008). Determination of the orientation distribution function in aligned single wall nanotube polymer nanocomposites by polarized Raman spectroscopy. *Journal of Applied Physics, 103*(7).
Pettermann, H. E., Bohm, H. J., & Rammerstorfer, F. G. (1997). Some direction dependent properties of matrix-inclusion type composites with given reinforcement orientation distributions. *Composites Part B, 28B*, 253–265.
Pujadas, P., Blanco, A., Cavalaro, S., de la Fuente, A., & Aguado, A. (2014a). Multidirectional double punch test to assess the post-cracking behaviour and fibre orientation of FRC. *Construction and Building Materials, 58*, 214–224.
Pujadas, P., Blanco, A., Cavalaro, S., de la Fuente, A., & Aguado, A. (2014b). Fibre distribution in macro-plastic fibre reinforced concrete slab-panels. *Construction and Building Materials, 64*, 496–503.
Redon, C., Chermant, L., Chermant, J. L., & Coster, M. (1998). Assessment of fibre orientation in reinforced concrete, using Fourier image transform. *Journal of Microscopy, 191*(3), 258–265.
Redon, C., Chermant, L., Chermant, J. L., & Coster, M. (1999). Automatic image analysis and morphology of fibre reinforced concrete. *Cement & Concrete Composites, 21*, 403–412.
Sevostianov, I. (2014). On the shape of effective inclusion in the Maxwell homogenization scheme for anisotropic elastic composites. *Mechanics of Materials, 75*, 45–59.
Sevostianov, I., & Giraud, A. (2013). Generalization of Maxwell homogenization scheme for elastic material containing inhomogeneities of diverse shape. *International Journal of Engineering Science, 64*, 23–36.
Sevostianov, I., & Kachanov, M. (1999). Compliance tensor of ellipsoidal inclusion. *International Journal of Fracture, 96*, L3–L7.
Sevostianov, I., & Kachanov, M. (2000). Modeling of the anisotropic elastic properties of plasma-sprayed coatings in relation to their microstructure. *Acta Materialia, 48*, 1361–1370.
Sevostianov, I., & Kachanov, M. (2002a). Elastic Compliances of Irregularly Shaped Cracks. *International Journal of Fracture, 114*, 245–257.
Sevostianov, I., & Kachanov, M. (2002b). Explicit cross-property correlations for anisotropic two-phase composite materials. *Journal of the Mechanics and Physics of Solids, 50*, 253–282.
Sevostianov, I., & Kachanov, M. (2007). Relations between compliances of inhomogeneities having the same shape but different elastic constants. *International Journal of Engineering Science, 45*, 797–806.
Sevostianov, I., & Kachanov, M. (2013). In *Non-interaction approximation in the problem of effective properties: 2013* (pp. 1–96). Springer. Chapter 1.
Sevostianov, I., & Kachanov, M. (2014). On some controversial issues in theories of effective properties. *Mechanics of Materials, 69*, 93–105.
Sevostianov, I., Levin, V., & Radi, E. (2016). Effective viscoelastic properties of short-fiber reinforced composites. *International Journal of Engineering Science, 100*, 61–73.
Stalling, D., Westerhof, M., & Hege, H.-C. (2005). Amira a Highly Interactive System for Visual Data Analysis. In Charles D. Hansen, & Chris R. Johnson (Eds.), *The visualization handbook* (pp. 749–767). Elsevier.
Suuronen, J.-P., Kallonen, A., Eik, M., Puttonen, J., Serimaa, R., & Herrmann, H. (2013). Analysis of short fibres orientation in steel fibre-reinforced concrete (SFRC) by X-ray tomography. *Journal of Material Science, 48*, 1358–1367.
Takao, Y., Chou, T. W., & Taya, M. (1982). Effective longitudinal young's modulus of misoriented short fiber composites. *Journal of Applied Mechanics, 49*, 536.
Tandon, G., & Weng, G. J. (1986). Average stress in the matrix and effective moduli of randomly oriented composites. *Composites Science and Technology, 27*(2), 111–132.
The Mathworks. MATLAB, Software, (2016). Natick, MA.
Tsuda, T., Ogasawara, T., Moon, S.-Y., Nakamotoc, K., Takedaa, N., Shimamurad, Y., et al. (2014). Three dimensional orientation angle distribution counting and calculation for the mechanical properties of aligned carbon nanotube/epoxy composites. *Composites Part A: Applied Science and Manufacturing, 65*, 1–9.
Turner, P. A., Signorelli, J. W., Bertinetti, M. A., & Bolmaro, R. E. (1999). Explicit method for calculating the effective properties and micromechanical stresses: An application to an alumina-SiC composite. *Philosophical Magazine A, 79*, 1379–1394.
Walpole, L. J. (1966). On bounds for the overall elastic moduli of inhomogeneous systems. *Journal of the Mechanics and Physics of Solids, 14*, 151–162.
Walpole, L. J. (1984). Fourth-rank tensors of the thirty-two crystal classes: Multiplication tables. *Proceedings of the Royal Society of London, A391*, 149–179 Volume 11, Issue 3, May 1991, Pages 251-256.
Zhu, Y. T., Blumenthal, W. R., & Lowe, T. C. (1997). Determination of nonsymmetric 3-D fiber orientation distribution and average fiber length in short-fiber composites. *Journal of Composite Materials, 31*(13), 1287–1301.
Zhupanska, O. I. (2013). The effect of orientational distribution of nanotubes on buckypaper nanocomposite mechanical properties. *Mechanics of Advanced Materials and Structures, 20*(1).